A Novel Approach to Surface Strain Measurement for Cylindrical Rock Specimens under Uniaxial Compression Using Distributed Fibre Optic Sensor Technology

by

Shao-Qun LIN

Department of Civil and Environmental Engineering

The Hong Kong Polytechnic University, Hong Kong, China

Email: shaoqun.lin@connect.polyu.hk

Dao-Yuan TAN (Corresponding Author)

Research Assistant Professor of

Department of Civil and Environmental Engineering

The Hong Kong Polytechnic University, Hong Kong, China

Email: rztdy2009@gmail.com

Jian-Hua YIN

Chair Professor of Soil Mechanics of

Department of Civil and Environmental Engineering

The Hong Kong Polytechnic University, Hong Kong, China

Email: cejhyin@polyu.edu.hk

and

Hua LI

College of Water Resource & Hydropower

Sichuan University, Chengdu, China

Email: huali@scu.edu.cn

Revised manuscript submitted to *Rock Mechanics and Rock Engineering* for possible publication as a research paper.

Sept 2021

Abstract: This study proposes a novel approach to surface strain measurement for cylindrical rock specimens subjected to uniaxial compression using distributed fibre optic sensing technology. The capability and accuracy of this approach in measuring the full-field strain distribution of a rock specimen have been verified by a series of uniaxial compressive strength (UCS) tests on cylindrical specimens of aluminium alloy, sandstone, and granite. By analysing the experimental results, this new approach also has the potential of being utilized to detect the potential failure locations and sequence through strain localization zone variations and estimation of the development of crack opening displacement and rock fracturing characteristics during the loading and unloading process. Detailed installation procedures are provided for this study for assistance in the use of this new approach. The boundary issue of fibre measurements is identified, and solved by extending the bonding length of the measuring fibre.

Keywords: Distributed fibre optic sensor; Strain field measurement; Uniaxial compression test; Failure analysis; Rock mechanics experiments

1. Introduction

At present, the uniaxial compression test is one of the basic and widely used laboratory test methods to estimate the mechanical properties and failure mechanisms of rocks through strain measurement (Basu et al. 2013; Kuhinek et al. 2011; Xie et al. 2011). Various technologies have been developed for strain measurement in laboratory tests, for example, electrical resistance strain gauges (ESG) (Clayton and Khatrush 1986; Montero et al. 2011), linear variable differential transformers (LVDTs) (Ibraim and Di Benedetto 2005), extensometers, fibre Bragg grating (FBG) (Sun et al. 2016; Zhang et al. 2018) and digital image correlation (DIC) (Abdulqader and Rizos 2020; Munoz et al. 2016). Even though traditional techniques, such as ESG, LVDT and extensometer are currently believed to be reliable methods for rock surface strain measurement, they can only provide strain measurement of a single point or at limited locations so that the mechanical properties of rock would be determined by a limited view of the strain field. Recently, due to the features of the fibre Bragg grating (FBG), including small size, immunity to electromagnetic interference, large-scale multiplexing capability, it has been applied widely in structural health monitoring (SHM), energy, and oil and gas downholes (Torres et al. 2011; Ye et al. 2014). This technology has been further extended to strain measurement for rock mechanics experiments. Sun et al. (2016) proposed novel fibre Bragg grating (FBG) sensor arrays for measuring dynamic strain-response of sandstone during UCS testing and their results were in good agreement with those of LVDTs. However, similar to other traditional methods, the fibre Bragg grating (FBG) also has the limitation of discrete and local measurements. Digital image correlation (DIC), as a non-intrusive method, has been introduced into strain field measurement because its capacity for measuring strain distribution within a monitoring window. Currently, the development from two-dimensional (2D) to three-dimensional (3D) DIC solved the measurement errors of 2D DIC caused by the relatively small out-of-plane motions and achieved full-field 3D surface strain measurement (Munoz and Taheri 2017; Zhang et al. 2018; Zhou et al. 2020). However, there are still some limitations for DIC, for example, dependence on strict external conditions, complicated post-test data processing, and limited strain resolution of 50με (Abdulqader and Rizos 2020).

Over the past several decades, distributed fibre optic sensing (DFOS), based on the Brillouin scattering or Rayleigh scattering work principle, has become increasingly popular for strain measurements in concrete bridges, composite structures, dams, and pipelines (Inaudi and Glisic 2008; Zou et al. 2004; Minardo et al. 2011; Sawicki et al. 2020), because it enables distributed monitoring along a sensing optical fibre and can further build a sensing network. An important parameter of this method is spatial resolution, which represents the strain measured at one point is the average value over the length of spatial resolution. For laboratory experiments, high spatial resolution is required for strain field measurement. Zhang et al. (2020) investigated the deformation and fracture propagation of a sandstone specimen under uniaxial compression using DFOS. The measuring fibre was mounted through a spiral bonding and the circumferential strain of sandstone was calculated approximately by the known Poisson's ratio. Xu et al. (2020) studied the dynamic strain response of the failure process of two cylindrical granite specimens under uniaxial compression using DFOS and spiral bonding was used to obtain circumferential strain. Uchida et al. (2015) utilized a single-mode fibre with coating and a flat jacket to measure the surface strains of an acrylic glass specimen in laboratory testing. The fully glued method and helical envelope configuration of measuring fibres were suggested, which provided the measurements of both axial and circumferential strains on the specimen surface successfully. Hegger (2021) proposed a monitoring configuration containing dense helical fibres and three circumferential loop fibres for strain measurement of grout specimens and granites in UCS tests, and axial extensometers were required to assist in calculating the axial strain. It can be found from existing researches that a satisfying measuring scheme for axial and lateral strains of rock surface is deficient and the strain transfer mechanism between specimen and optical fibre is in need of investigation.

This study aims to propose a novel approach to surface strain measurement for cylindrical rock specimens using distributed fibre optic sensing technology and further investigate its potential for measuring rock crack opening displacement for rock fracturing characteristics research. First, a UCS test on an aluminium alloy specimen was conducted to study the feasibility and reliability of the distributed fibre optic sensor and corresponding installation method. Afterwards, the optical fibre

sensing approach was applied for strain field measurement for a cylindrical sandstone specimen under uniaxial compression. Failure behaviour of the sandstone is analysed based on the surface strain development under axial loading. Furthermore, the approach was applied to estimate the crack opening displacement of a granite specimen under uniaxial compression. Finally, a strain transferring mechanical model is introduced to discuss the imperfect strain transference at the boundaries of the measuring fibre, which can be solved by extending the bonding length of the measuring fibre.

2. Principle of optical frequency domain reflectometry (OFDR) sensing technology

Rayleigh scattering is a quasi-elastic optical scattering phenomenon existing in optical fibre. For a given fibre with a constant refractive index, the Rayleigh backscatter can be seen as a random and individual fingerprint distributed along the fibre length. External temperature or strain variation in the fibre can induce a shift in the local spectrum (Barrias et al. 2019). Based on this, the OFDR sensing technology was developed. As shown in Fig. 1a, the linear sweep continuous light output from a tunable laser source is divided into two paths by the optical coupler and one is used as the reference light and reflected through a mirror, while the other is used as the measurement light. When the measurement light propagates in the measuring fibre of a specimen, Rayleigh backscattered light is generated. Afterwards, the scattered light is mixed with the reference light by the optical coupler, which produces beat frequency interference that can be received and demodulated by the photoelectric detector to obtain the strain or temperature changes along the length of the measuring fibre. Specifically, the relation between the spectral shift and the strain and temperature changes can be expressed as follows:

$$\Delta v = C_\varepsilon \Delta\varepsilon + C_T \Delta T \tag{1}$$

where Δv is the Rayleigh spectrum shift, $\Delta\varepsilon$ is the strain change in the fibre, ΔT is the temperature change for the fibre, C_ε and C_T are constants related to strain change and temperature change, respectively. For a standard single-mode fibre, C_ε and C_T were calibrated as -0.15 GHz/με and -1.25 GHz/°C (Wu et al. 2020), respectively. The OFDR sensing technology adopted in this study can achieve

a spatial resolution of 1 mm in a sensing range of 100 m with an outstanding measuring accuracy of about ± 0.1 ℃ or ± 1 με, which is fully suitable for strain measurement and micro-crack detection in rocks in laboratory experiments.

3. Verification of distributed optical fibre sensing technology for strain measurement

To study the feasibility and reliability of the fibre optic sensing technology for surface strain field measurement on cylindrical specimens, a UCS test of an aluminium alloy specimen is introduced in this section. A homogeneous cylindrical 5052 aluminium alloy specimen with a diameter of 70.6mm and a height of 142mm was utilized to carry out the UCS test. Corning SMF-28E(R) Fibre without thick coatings or jackets was chosen as the sensing fibre to avoid the buffering influence of protective coatings or jackets on measurements and ensure its effect on the mechanical performance of host material can be neglected. This type of fibre only consists of silica core, cladding and protective coating, with an overall diameter of 250 μm, as shown in Fig. 1b.

3.1 Fibre installation principle and process

For measuring the lateral strain and axial strain on the aluminium alloy specimen surface, a surface-bonded measurement layout with five hoop fibres and a spiral fibre is proposed, as shown in Fig. 2a. The hoop fibres are aimed to measure the lateral strain distribution on the aluminium alloy specimen surface, while the spiral fibre is utilized to obtain the axial strain. Based on the small deformation theory, the strains measured by two intersected fibres can be transformed into the lateral strain and axial strain as follows (Uchida et al. 2015):

$$\varepsilon_L = \frac{\varepsilon_1 - \varepsilon_2 \left(\frac{\sin\theta_1}{\sin\theta_2} \right)^2}{1 - \left(\frac{\sin\theta_1}{\sin\theta_2} \right)^2} \tag{2}$$

$$\varepsilon_A = \frac{\varepsilon_1 - \varepsilon_2 \left(\frac{\cos\theta_1}{\cos\theta_2} \right)^2}{1 - \left(\frac{\cos\theta_1}{\cos\theta_2} \right)^2} \tag{3}$$

where ε_L is the lateral strain, ε_A is the axial strain, θ_1 and θ_2 are the inclined angles of the optical fibres and ε_1 and ε_2 are the strains in the respective fibres.

In this paper, the installation angles of five hoop fibres are set to zero so that the lateral strain distribution can be obtained directly according to Eq. (2). On the other hand, the installation angle of the spiral fibre is determined by Eq. (4).

$$\theta \leq \arctan\sqrt{\upsilon} \tag{4}$$

where θ is the installation angle, and υ is the Poisson's ratio of the specimens' material.

Under an ideal elastic deformation, the calculated angle can keep the spiral fibre in tension during the loading procedure. For a specimen with an unknown Poisson's ratio, a low value of Poisson's ratio is suggested to calculate the installation angle. Therefore, the axial strain of the specimen can be calculated through the measurements from both hoop fibres and the spiral fibre using Eq. (3).

Specifically, five hoop fibres marked as 'L1~L5' in Fig. 2a were mounted on the aluminium alloy specimen at an interval of 25 mm, and 'L1' and 'L5' were located at 21 mm from the bottom and top of the specimen, respectively. The spiral fibre marked as 'S' intersected all hoop fibres at an angle of 24.3°. Most importantly, a section of slack fibre was set up between each measuring fibre, and a loose fibre coil was reserved between the 'S' and 'L5' fibre. The slack fibres were designed to distinguish different measuring fibres and position the measured strains assuming that the slack fibres were

mechanical strain free, which can also be utilized to conduct temperature compensation for measuring fibres in case the temperature change is significant during testing.

To achieve this layout, a platform was designed and shown in Fig. 3, which combined a V-shaped groove, rubber mats, and a dead weight. The rubbers were utilized to support the specimen, which prevented the measuring and slack fibres from being damaged. The dead weight temporarily fixed to the fibre by tapes was used to apply pretension on the measuring fibre during the mounting procedure. After that, CN cyanoacrylate adhesive (Tokyo Measuring Instruments Lab, Japan) with short curing time was used to position the measuring fibres, and epoxy adhesive DP460 (3M, Minnesota, US) was used to protect the fibres and further sufficiently bond the measuring fibres to the specimen. Fig.2b shows the aluminium alloy specimen with all fibres installed.

3.2 Test results

The uniaxial compression test was carried out under load-controlled mode at a rate of 1.0 kN/s and the maximum loading was up to 900 kN. The strain field of the aluminium alloy specimen was measured every 5 sec by an OFDR-based interrogator (OSI-I, Junlong Technology Ltd., China) with a spatial resolution of 1 mm. Due to the short testing period (900 seconds) and temperature control in the constant temperature laboratory, the temperature during the test procedure was assumed to be constant.

The strains recorded by the six fibres are shown in Fig. 4a and in total eighteen loading steps are plotted with a loading interval of 50 kN. As can be seen, the measured strain of each fibre section is well separated and increases uniformly with loading. Maximum strain measurements for the five hoop fibres are close at each loading step because of the homogeneous nature of the specimen, especially those measurements of ‘L2~L4’ fibres, which were less affected by the end friction effect (Peng and Johnson 1972). For fibres ‘L2~L5’, the measured strains tend to be more uniform along the perimeter with

increased loading. That is mainly due to the insufficient contact between the fibres and the specimen at low loading stages. Considering that we did not provide a stable pretension for the measuring fibres on this aluminium cylinder, the pretension of measuring fibres throughout the installation process is essential and can be guaranteed by the dead weight mentioned above to achieve accurate strain measurement during the lower loading stages.

For further verification of the reliability of measurements, the lateral and axial strains on the central point on the specimen surface (shown in Fig. 2a) were calculated based on Eq. (2) and Eq. (3). The measurements from the hoop fibre 'L3' and spiral fibre 'S' were utilized in the calculation. Then, the Poisson's ratio υ of the specimen can be obtained. Fig. 4b shows the strain-stress and υ-stress curves of the specimen in the uniaxial compression test. The calculated Poisson's ratio υ increases from about 0.20 at the early loading stage and stabilizes at the value of 0.35 when the axial stress reaches 150 MPa. The obtained Poisson's ratio is in good agreement for 5052 aluminium alloy (0.33 given by Fitch (1963)), which indicates that the surface measurement layout and calculation method introduced in this section are suitable for strain measurement of cylindrical specimens.

4. Surface strain field measurement of a sandstone sample

To verify reliability and accuracy for strain field measurement using this fibre optic sensing technology in rock mechanics laboratory experiments, a UCS test on a sandstone specimen with measuring fibres was performed. The test results are plotted and analysed in this section.

4.1 Experimental setup

The specimen used in this experiment was cored from fine-grained sandstone (Sichuan Zigong, Southwestern China) and its diameter and height are 68.7mm and 140.0 mm, respectively. The specimen was prepared in accordance with ASTM (2008). The end surfaces were ground to meet the

specified shape tolerances. Before the installation of sensors, the side surface of sandstone was equally divided into four regions by vertical lines drawn in pencil, and the regions were marked by Roman numerals, as shown in Fig. 5a.

Along with the hoop fibres and a spiral fibre, two sets of resistance strain gauges (Chengdu Electronic Measuring Sensing Technology Co., Ltd., China) were also attached to the surface of the sandstone for strain verification. Specifically, four strain gauges were placed in the middle position of the I~IV regions of the sandstone. Two of them marked as 'SG1' and 'SG3' were glued in the axial direction of I and III regions for axial strain measurement, and the other two marked as 'SG2' and 'SG4' were glued in the lateral direction of the II and IV regions for lateral strain measurement.

As with the measurement layout on the aluminium alloy specimen, there were five hoop fibres marked as 'L0~L4' and a spiral fibre marked as 'S' used to measure the lateral strain and axial strain, respectively. It is worth noting that the hoop fibre in the middle position was removed due to the limited space after the positioning of the four strain gauges, and another hoop fibre marked as 'L0' was mounted at a distance of 20mm from the bottom with a length of 1.5 times the sandstone perimeter. The measurements from 'L0' were aimed to investigate the boundary of fibre measurements, which will be reviewed in the Discussion section. The installation intervals of five hoop fibres are shown in Fig. 5a. The spiral fibre intersected 'L1' to 'L4' at an inclined angle of 20.3° calculated by Eq. (4). Throughout the installation process, the designed platform was used to assist in installing and pre-tensioning the measuring fibres. Furthermore, the CN cyanoacrylate adhesive and epoxy adhesive DP460 were applied for positioning, bonding, and protecting the measuring fibres.

In this UCS test, the loading was carried out under the load-controlled mode at a rate of 0.1 kN/s until the sandstone specimen failed. During the test process, the OFDR-based interrogator was used for data collection under settings of spatial resolution of 1 mm and a data collection frequency of 0.2 Hz, while

a datalogger with a logging frequency of 1.0 Hz was used to collect data from the strain gauges. With temperature control measures applied, the temperature changes in the laboratory were negligible. The data collection was started from a preloading stage with the axial stress of 1.4MPa.

4.2 Comparison of results between strain gauges and measuring fibres

The strain history of the sandstone collected by the four strain gauges are present in Fig. 6 and the volumetric strain was calculated using $\varepsilon_v = \varepsilon_{SG1(3)} + 2\varepsilon_{SG4(2)}$. It can be found that the strain responses of strain gauges in the lateral or axial direction show similar trend under different axial stresses and the two curves for the volumetric strain for the sandstone almost overlap. Moreover, the crack damage stress threshold σ_{cd} and uniaxial compressive strength σ_{ucs} of the sandstone are 24.3 MPa and 49.9 MPa, respectively, where σ_{cd} is the axial stress threshold above which crack propagation tends to be unstable, and σ_{ucs} is the uniaxial compressive strength (Xue et al. 2014).

The measurements of 'L1~L4' and 'S' fibres under 25 loading steps are presented in Fig. 7 and the axial stress increment is 2.0 MPa. Different measurements along 'L1~L4' fibres under the same loading step indicate that the local deformation differences of the sandstone were detected. The lateral measured strains of 'L2' and 'L3' fibres at the same lateral locations as 'SG2' and 'SG4' are plotted to compare with the results from SG2 and SG4. The selected sensing points of fibres are marked as 'L2-SG2', 'L2-SG4', 'L3-SG2' and 'L3-SG4', as shown in Fig. 5a. The axial strains of the sensing point marked as 'S-L3' in Fig. 5a are calculated by Eq. (3) using the measurements of the 'S' and 'L3' fibres. Furthermore, the axial strains of the sensing point marked as 'S-SG2' in Fig. 5a are calculated by Eq. (3) using the measurements from the 'S' fibre and 'SG2'. Therefore, six stress-strain curves are obtained by the measuring fibres and shown in Fig. 6.

The six lateral strain curves for the sandstone obtained by strain gauges and measuring fibres show a similar trend under axial compression. The values of 'SG4' and 'L2-SG2' are almost consistent, while those of the other four curves are different due to local differences of lateral strain on the sandstone surface. In addition, after the sandstone enters the unstable crack growth stage, the lateral strains for these strain gauges become larger than those of the measuring fibres because strain localization occurs near the middle of the sandstone (see section 4.3).

The axial strains from both 'S-SG2' and 'S-L3' fit well with 'SG1', especially when the axial stress is smaller than the crack damage stress threshold σ_{cd}. Different from the measured lateral strain, the measured axial strains of 'S-SG2', 'S-L3' and 'SG1' at different positions on the sandstone still show good agreement with each other during the early stage of unstable crack growth. However, during the post-stage of unstable crack growth of the sandstone, the measurements of 'S-SG2' and 'S-L3' become larger than those of the 'SG1' and 'SG3' under the same axial stress and the trend continues until the failure of sandstone occurs. Furthermore, it can be deduced from the measurements of 'S-SG2' and 'S-L3' that their positions fall into failure earlier than those of 'SG1' and 'SG3'. Therefore, the uniaxial compressive strength, σ_{ucs} given by strain gauges is slightly overestimated. The distributed optical fibre sensing can be a more credible technology to determine the crack developing stage of the sandstone than traditional strain gauges with limited sensing areas.

4.3 Strain field measurement and failure analysis of the sandstone

Throughout the UCS test, the lateral strains in the sandstone in the circumferential direction were collected by the 'L1~L4' fibres at different heights. As shown in Fig. 8, the strain distributions on the sandstone surface at three typical loading stages were selected to study the capacity of measuring fibres for detecting and quantifying strain localization.

When the axial stress is 24.0 MPa, the maximum lateral strain on the sandstone surface is about 750 με and locates in the II region of the 'L1' fibre (see Fig. 8a). In this loading stage, the lateral strain of sandstone concentrates on II and III regions of 'L2' and 'L1' fibres. This strain distribution pattern remains stable from the stable crack growth stage to the post-stage of the unstable crack growth.

When the axial stress is up to 44.0 MPa, the maximum lateral strain on the sandstone surface increases to 2500 με and its location moves to the II region of 'L2' fibre (see Fig. 8b). In addition, the maximum lateral strains of 'L3' fibre and 'L1' fibre are almost equal, which means the core of the lateral strain localization zone has moved up the sandstone.

The third typical strain distribution figure was obtained under the axial stress of 48.0 MPa. The maximum lateral strain on the sandstone surface further increases to 4000 με and its location remains unchanged (see Fig. 8c). Even though the axial stress only increases 4.0 MPa compared with that in Fig. 8b, the maximum lateral strain has a significant growth because the axial stress is about to reach the uniaxial compressive strength of the sandstone. Meanwhile, the maximum lateral strain of 'L3' fibre becomes larger than that of 'L1' fibre which indicates the core of the lateral strain localization zone has finally moved to the centre of the sandstone.

On the whole, the strain localization zone of lateral strain mainly occurs in the II region of the sandstone and its core moves from bottom to centre with the increase of axial stress. The strains of 'L4' fibre are smaller than those of 'L1~L3' fibres throughout the UCS test due to the inevitable end friction effect in this test (Peng and Johnson 1972).

The strain localization on the sandstone surface can be seen as the potential failure zone. Hence, the relationship between the strain distributions given by measuring fibres and the failure mode of the

sandstone is investigated to further verify the capacity of measuring fibres for detecting strain localization and to understand the failure behaviour of the sandstone. To detect the potential failure locations in the sandstone, strain localization characteristics under three different axial stresses are shown in Figs. 9a ~ 9c and compared with the photo of sandstone failure mode in Fig. 9d. It is worth noting that at each height level in Fig. 9a ~ 9c, for 'L1~L4' fibres, only the lateral strains larger than 95% of maximum strains of that height are plotted for clear observation of the strain localization at different heights. For 'S' fibres, only the measured strains larger than 95% of its maximum strains are plotted.

It can be found from Fig. 9d that the failure mode of sandstone is mainly a form of conjugate X-shaped shear failure (Basu et al. 2013; Liang et al. 2015; Yuan et al. 2020), and two shear cracks are marked as 'C1' and 'C2'. As indicated in Fig. 9a, when the axial stress is 24.0 MPa and the sandstone is under stable crack growth stage, the strain localization detected by 'L1~L3' and 'S' fibres is able to roughly reflect the location of the 'C1' crack, while no significant strain localization related to the 'C2' crack is observed.

When the sandstone reaches the post-stage of unstable crack growth under axial stress of 48.0 MPa, the strain localization of 'L1~L3' and 'S' fibres become more significant in Fig. 9b, which means the strain localization of the sandstone surface further develops. In this stage, the strain localization detected by 'L1~L3' and 'S' fibres fits well with the location of the 'C1' crack, and the strain localization detected by 'L4' fibre tends to be close to the distribution of 'C2' crack. Hence, it can be inferred that the strain localization of the 'C1' crack grows earlier than that of the 'C2' crack.

Before the sandstone falls into failure, the latest data collected by measuring fibres are shown in Fig. 9c. Obvious strain localization along four heights of the sandstone can be observed. Most importantly, the strain localization detected by 'L4' fibre is covered by the location of 'C2' crack which means the

strain localization of ‘C2’ crack has a significant development after the stage of axial stress of 48.0 MPa. In addition, there is no strain localization detected by measuring fibres in the location of ‘C2’ crack which is below the centre of the sandstone, and this can be attributed to the ‘C2’ crack initiating from the upper section (L4), propagates as a critical crack and finally generates shear failure.

Furthermore, the strain localization of ‘L1~L3’ fibres has a small shift to the left before sandstone failure. The strain localization of ‘L3’ fibre is influenced by the overall location of ‘C1’ and ‘C2’ cracks and shifts to the centre of these two cracks in this stage because of the strain localization development of the ‘C2’ crack. The shift of the strain localization of ‘L2’ fibre makes it fit better with the location of the ‘C1’ crack and further verifies that the strain localization of ‘C2’ crack below the centre of the sandstone will still not occur. The strain localization of the ‘L1’ fibre moves far away from the ‘C1’ crack location at this stage, which shows that the final location of the ‘C1’ crack does not pass through the height below the ‘L1’ fibre.

Therefore, using measuring fibres to investigate the strain field of a sandstone in the UCS test along with the failure behaviour is promising. In this test, only four lateral strain fibres were used to show the feasibility of the DFOS method. By densifying the measuring fibres, more accurate measurement of the surface strain distribution and detailed detection of strain localization can be achieved.

5. Crack opening displacement measurement in a granite sample

The reliable installation method and desirable measurement accuracy of optical fibres for rock UCS tests were discussed in a preliminary test using an aluminium alloy specimen. After that, the optical fibres were utilized for surface strain field measurement of sandstone in a UCS test. Compared with strain gauges, the measuring fibres can provide accurate measurements of surface strain distribution on rock specimens. By densifying the arrangement of measuring fibres, this method shows great potential

for accurate surface strain measurement of rock specimens in UCS and triaxial tests. In general, a triaxial compression test has a triaxial cell to apply the confining pressure for a rock specimen through the hydraulic fluid (ISRM 1978). Given that the measuring fibres are immune to the confining pressure, the hydraulic fluid and electromagnetic interference, it is reasonable to expect the DFOS method to show a promising performance in surface strain field measurement of rock specimens in triaxial compression tests.

Beside the detection and quantification of strain localization on the surface, rock fracturing characteristics, for example, crack opening displacement (COD), are important in rock mechanical experiments. The COD is mainly investigated through Digital Imaging Correlation (DIC), Acoustic Emission (AE), Fiber Bragg Grating (FBG) (Zhang et al. 2018). The potential of distributed optical fibre sensing (DFOS) for measuring the COD of rocks has been rarely studied. Another UCS test on a granite sample was conducted to investigate the feasibility of the DFOS method for COD measurement in a rock. The diameter and height of the granite cylindrical sample were 69.2 mm and 140.3 mm, respectively. In this test, the maximum axial stress was set to 80.0 MPa and tensile wing cracks were found to develop on the granite surface.

To quantify the COD of the granite cracks, a strain transferring model for optical fibres installed on a fractured material is introduced. This model (see Fig. 10a) is further developed from Li's model by regarding a crack as an additional local discontinuity in the measured material deformation field (Li et al. 2012). The model has been verified by comparing its calculation results with the experimental results for concrete structures (Bassil et al. 2020; Feng et al. 2019). Specifically, during the cracking situation, the strain transfer function along a measuring fibre at a given x coordinate can be expressed as follows:

$$\varepsilon_m = \varepsilon_{rock} + \sum_{i=1}^{n} \lambda \frac{COD_i}{2} e^{-\lambda|x-x_i|} \tag{5}$$

$$\lambda^2 = \frac{2G_e}{r_f^2 E_f \ln\left(\frac{r_e}{r_f}\right)} \tag{6}$$

where ε_{rock} is the basal strain on the rock surface, λ is the strain lag parameter, COD_i is the opening displacement of each crack i, n is the total numbers of cracks, and x_i is the position of each crack, G_e is the shear modulus of the epoxy adhesive, E_f is the elastic modulus of fibre core, r_f and r_e are the radii of the fibre and epoxy adhesive layer, respectively.

The measurement of a measuring fibre under the axial stress of 80.0 MPa is utilized to fit the strain transfer function of cracking and obtain the opening displacement for each crack. The values of the parameters for the measuring fibres are provided in Table 1. Here, the buffering influence of the protective coating with a thickness of 125 μm is negligible compared with the epoxy layer with a diameter of about 2.0 mm. The ε_{rock} is about 200 με obtained by fitting the strain distribution in the measuring fibre using Eq. (5). As shown in Fig. 10b, the measured strain indicates three cracks occurred along the granite perimeter, and they can also be found from three local photos of the II ~ IV regions. Based on Eq. (5) and the location of each crack, the maximum opening displacements of three cracks were computed with the values of 132.2 μm, 114.6 μm and 16.4 μm, respectively, and the strain distribution curve after fitting was also obtained. For further verifying the accuracy of the fitting results, the residuals between the measured and computed strain are calculated and also plotted in Fig. 10b. It can be observed that the residuals along the measured length are between -150 με and 100 με, and the maximum residual located in the position of the crack of III region is only 7.2% of the measured strain.

The COD fitting results of measurements collected by the measuring fibre under different loadings are shown in Fig. 10c to investigate the COD development of three cracks. As shown in Fig. 10c, the cracks locating in II and III regions initiate when the granite is subjected to the axial stress of 8.4 MPa and their COD increases linearly following the development of axial stress. When the axial stress exceeds

44.0 MPa, the crack located in the IV region expands and its opening displacement increases linearly. Due to the occurrence of the third crack, the COD of the other two cracks becomes stable until the axial stress exceeds 48.0 MPa and then follows exponential growth.

When the axial stress reached 80.0 MPa, the UCS test was ended, and the granite was unloaded instantly. It can be observed from Fig. 10c that even though the external force is removed, three cracks are not completely closed and there are some COD residuals. The computed results indicate that the final values of COD of three cracks are 43.4 μm, 43.7 μm and 6.7 μm, respectively. Hence, the quantification of COD on the rock specimen under compression shows the potential of this measurement method being used to study fracturing behaviour of rock.

6. Discussion

In this paper, optical fibres were bonded onto the surface of specimens with epoxy adhesive for increasing the efficiency of strain transference from the rock surface to the measuring fibre. The epoxy adhesive called 3M DP460 was utilized here due to its excellent shear and peel strength. However, compared with the silica core of the fibres, it has a relatively lower elastic modulus which can result in shear stresses between the fibre core and the measured specimen, and leads to imperfect strain transferring near the boundary of the measuring fibre. A strain transferring mechanical model (see Fig. 11a) developed by Li et al. (2012) is introduced to investigate this problem. The strain transfer rate along a measuring fibre at a given x coordinate can be expressed as follows:

$$R = 1 - \frac{\cosh\left(\lambda x\right)}{\cosh\left(\lambda L/2\right)} \tag{7}$$

where R is the strain transfer rate, λ is the strain lag parameter which can be calculated through Eq. (6), L is the bonding length of the measuring fibre, x is the distance from the midpoint of the measuring

fibre, namely, $-L/2 \le x \le L/2$, G_e is the shear modulus of the epoxy adhesive, E_f is the elastic modulus of the fibre core, r_f and r_e are the radii of the fibre and epoxy adhesive layer, respectively.

As known from the equations, two parameters are controllable during the installation process of the measuring fibres, which are the radius of the epoxy adhesive layer and the bonding length. In the UCS test on the sandstone, the radius of the epoxy adhesive layer was kept about 1.0 mm and the bonding length of the 'L1~L4' fibres was about 215.8 mm, namely the same as the perimeter of the sandstone, while the bonding length of the 'L0' fibre was about 323.7 mm, namely 1.5 times of the perimeter. The strain transfer rate along the measuring fibre under seven different situations (see table 2) was calculated and is presented in Fig. 11b. In this figure, '1.0 L/250 E' means that the bonding length of measuring fibre is equal to the perimeter of the sandstone and the radius of the epoxy adhesive layer is 250 μm. It is worth noting that the length possessing more than 95% of the strain transfer rate is regarded as the effective measuring length of the measuring fibre here.

In Fig. 11b, when the bonding length is kept the same as the perimeter of the sandstone, the effective measuring length decreases with the increase of the radius of the epoxy adhesive layer. The effective length is only 83.3% of the perimeter length of the sandstone when the radius of the epoxy adhesive layer is 1.0 mm. However, it is difficult to make the radius of the epoxy adhesive layer smaller than 1.0 mm in the installation process. When the bonding length is 1.25 times or 1.5 times the perimeter, the measured strain along the perimeter length can effectively reflect the realistic strain in this UCS test. Especially, when the bonding length is 1.5 times the perimeter, the strain transfer rates along the perimeter length exceed 99.9% theoretically. Furthermore, effectiveness for elimination of the boundary effect of fibre measurements by adding bonding length is studied by arranging an additional fibre 'L0' in the UCS test of sandstone. The strain measurements of 'L1' and 'L0' fibre are compared in Fig. 12. It can be observed that the measurements close to the boundary of 'L1'fibre significantly drop, while those close to the boundary of 'L0' fibre keep stable. Therefore, to eliminate the boundary effect of

fibre measurements, it is suggested to set up the measuring fibre with an extra bonding length (calculated by the introduced model) at two ends and make the epoxy adhesive layer as thin as possible.

7. Conclusion

This paper introduces a novel approach to strain field measurement on the surface of rock specimens in uniaxial compression tests using distributed fibre optic sensing (DFOS) technology with high strain accuracy and high spatial resolution. The test results for three UCS tests using different materials, aluminium alloy, sandstone, and granite, are analysed, and the following findings can be summarized as follows:

(a) The proposed approach is effective to measure the lateral and axial strains with high precision of ± 1 με on the surface of cylinder rock specimen subjected to uniaxial compression.

(b) The lateral and axial strains of sandstone measured by optical fibres and strain gauges show a good agreement with each other. The lateral strains measured by strain gauges become larger than those by fibres because strain localization occurs at the centre of the sandstone. The axial strains measured by optical fibres become larger than those from strain gauges at the post-stage of unstable crack growth because the local measurement by the strain gauge cannot always provide a satisfactory result. By comparison, the distributed optical fibre sensing method can determine the crack developing stage of the sandstone more accurately than the local measurement provided by traditional strain gauges.

(c) Through the measured lateral strains with optical fibres, the strain localization on the sandstone surface was identified. It can be inferred that the strain localization zone moves from bottom to centre with increase of axial stress. In addition, based on the quantification of strain localization at different heights in the sandstone, the conjugate X-shaped shear failure was detected, which fits well with the photograph. Most importantly, the positional variation of lateral strain localization indicates the possible sequence of crack occurrence.

(d) The opening displacements of three cracks occurring on the surface of the granite specimen were calculated with the maximum values of 132.2 μm, 114.6 μm and 16.4 μm, respectively, based on the introduced strain transferring mechanical model, which verifies the feasibility of applying DFOS technology for COD measurement in rock experiments.

(e) The proposed installation procedures for measuring fibres are reliable, and the boundary issue of optical fibre measurements can be eliminated by extending the bonding length of the measuring fibre and making the epoxy adhesive layer as thin as practicable.

The promising performance of this novel approach to surface strain measurement for cylinder rock samples has demonstrated immense potential in local deformation monitoring, especially in those concerning non-uniform deformation. For example, triaxial compression tests of natural rocks for measuring elastic modulus and predicting the location of potential macrocrack emergence, direct shear tests or biaxial tests of rough joints for localizing slip initiation, and creep tests of filled joints or rock masses for monitoring time-dependent creep behavior.

Data Availability Statement

All data, models, and code generated or used in this study are available from the corresponding author upon reasonable request.

Acknowledgement

The work in this paper is supported by a Research Impact Fund (RIF) project (R5037-18), a Theme-based Research Scheme Fund (TRS) project (T22-502/18-R), and three General Research Fund (GRF) projects (PolyU 152209/17E; PolyU 152179/18E; PolyU 152130/19E) from Research Grants Council (RGC) of Hong Kong SAR.

References

ASTM D4543–08 (2008) Standard practices for preparing rock core as cylindrical test specimens and verifying conformance to dimensional and shape tolerances. In Annual Book of ASTM Standards. West Conshohocken, PA: ASTM International

Abdulqader A, Rizos DC (2020) Advantages of using digital image correlation techniques in uniaxial compression tests. Results Eng 6: 100109. https://doi.org/10.1016/j.rineng.2020.100109

Basu A, Mishra D, Roychowdhury K (2013) Rock failure modes under uniaxial compression, Brazilian, and point load tests. B Eng Geol Environ 72(3): 457-475. https://doi.org/10.1007/s10064-013-0505-4

Barrias A, Casas JR, Villalba S (2019) Distributed optical fibre sensors in concrete structures: Performance of bonding adhesives and influence of spatial resolution. Strcut Control Hlth 26(3): e2310. https://doi.org/10.1002/stc.2310

Bassil A, Chapeleau X, Leduc D, Abraham O (2020) Concrete Crack Monitoring Using a Novel Strain Transfer Model for Distributed Fiber Optics Sensors. Sensors (Basel) 20(8): 2220. https://doi.org/10.3390/s20082220

Clayton C, Khatrush S (1986) A new device for measuring local axial strains on triaxial specimens. Géotechnique 36(4): 593-597. https://doi.org/10.1680/geot.1986.36.4.593

Fitch AH (1963) Observation of Elastic-Pulse Propagation in Axially Symmetric and Nonaxially Symmetric Longitudinal Modes of Hollow Cylinders. The Journal of the Acoustical Society of America 35(5): 706-708. https://doi.org/10.1121/1.1918594

Feng WQ, Yin JH, Borana L, Qin JQ, Wu PC, Yang, JL (2019) A network theory for BOTDA measurement of deformations of geotechnical structures and error analysis. Measurement 146: 618-627. https://doi.org/10.1016/j.measurement.2019.07.010

Hegger SA (2021) The Application of Distributed Optical Sensing to Measure the Full-Field Strain Response of Uniaxial Compression Test Specimens. Dissertation, Queen's University.

ISRM (1978) Commission on standardization of laboratory and field tests. Suggested methods for determining the strength of rock materials in triaxial compression. Int J Rock Mech Min Sci.Geomech Abstr 15: 47-51.

Ibraim E, Di Benedetto H (2005) New local system of measurement of axial strains for triaxial apparatus using LVDT. Geotech Test J 28(5): 436-444. https://doi.org/10.1520/GTJ11630

Inaudi D, Glisic B (2008) Overview of fibre optic sensing applications to structural health monitoring. Proc., Symposium on Deformation Measurement and Analysis 1-10.

Kuhinek D, Zorić I, Hrženjak P (2011) Measurement uncertainty in testing of uniaxial compressive strength and deformability of rock samples. Meas Sci Rev 11(4): 112-117.

Li D, Ren L, Li H (2012) Mechanical property and strain transferring mechanism in optical fiber sensors. Fiber optic sensors. IntechOpen.

Liang CY, Zhang QB, Li X, Xin P (2015) The effect of specimen shape and strain rate on uniaxial compressive behavior of rock material. B Eng Geol Environ 75(4): 1669-1681. https://doi.org/10.1007/s10064-015-0811-0

Minardo A, Bernini R, Amato L, Zeni L (2011) Bridge monitoring using Brillouin fiber-optic sensors. IEEE Sensors Journal 12(1): 145-150. https://doi.org/10.1109/JSEN.2011.2141985

Montero W, Farag R, Diaz V, Ramirez M, Boada B (2011) Uncertainties associated with strain-measuring systems using resistance strain gauges. The Journal of Strain Analysis for Engineering Design 46(1): 1-13. https://doi.org/10.1243/03093247JSA661

Munoz H, Taheri A, Chanda EK (2016) Pre-peak and post-peak rock strain characteristics during uniaxial compression by 3D digital image correlation. Rock Mech Rock Eng 49(7): 2541-2554. https://doi.org/10.1007/s00603-016-0935-y

Munoz H, Taheri A (2017) Specimen aspect ratio and progressive field strain development of sandstone under uniaxial compression by three-dimensional digital image correlation. J Rock Mech Geotech 9(4): 599-610. https://doi.org/10.1016/j.jrmge.2017.01.005

Peng S, Johnson AM (1972) Crack growth and faulting in cylindrical specimens of Chelmsford granite. International Journal of Rock Mechanics and Mining Sciences & Geomechanics Abstracts 9(1): 37-86. https://doi.org/10.1016/0148-9062(72)90050-2

Sun Y, Li Q, Yang D, Fan C, Sun A (2016) Investigation of the dynamic strain responses of sandstone using multichannel fiber-optic sensor arrays. Eng Geol 213: 1-10. https://doi.org/10.1016/j.enggeo.2016.08.008

Sawicki B, Bassil A, Bruhwiler E, Chapeleau X, Leduc D (2020) Detection and Measurement of Matrix Discontinuities in UHPFRC by Means of Distributed Fiber Optics Sensing. Sensors (Basel) 20(14): 3883. https://doi.org/10.3390/s20143883

Torres B, Payá-Zaforteza I, Calderón PA, Adam JM (2011) Analysis of the strain transfer in a new FBG sensor for structural health monitoring. Eng Struct 33(2): 539-548. https://doi.org/10.1016/j.engstruct.2010.11.012

Uchida S, Levenberg E, Klar A (2015) On-specimen strain measurement with fiber optic distributed sensing. Measurement 60: 104-113. https://doi.org/10.1016/j.measurement.2014.09.054

Wu J, Liu H, Yang P, Tang B, Wei G. (2020) Quantitative strain measurement and crack opening estimate in concrete structures based on OFDR technology. Opt Fiber Technol 60: 102354. https://doi.org/10.1016/j.yofte.2020.102354

Xie H, Pei J, Zuo J, Zhang R (2011) Investigation of mechanical properties of fractured marbles by uniaxial compression tests. J Rock Mech Geotech 3(4): 302-313. https://doi.org/10.3724/SP.J.1235.2011.00302

Xue L, Qi M, Qin S, Li G, Li P, Wang M (2014) A potential strain indicator for brittle failure prediction of low-porosity rock: Part I—experimental studies based on the uniaxial compression test. Rock Mech Rock Eng 48(5): 1763-1772. https://doi.org/10.1007/s00603-014-0675-9

Xu S, Wang S, Zhang P, Yang D, Sun B (2020) Study on strain characterization and failure location of rock fracture process using distributed optical fiber under uniaxial compression. Sensors 20(14): 3853. https://doi.org/10.3390/s20143853

Ye XW, Su YH, Han JP (2014) Structural health monitoring of civil infrastructure using optical fiber sensing technology: A comprehensive review. The Scientific World Journal. https://doi.org/10.1155/2014/652329

Yuan C, Guo Y, Wang W, Cao L, Fan L, Huang C (2020) Study on "Triaxial Loading-Unloading-Uniaxial Loading" and Microscopic Damage Test of Sandstone. Front Earth Sc-switz 8: 78. https://doi.org/10.3389/feart.2020.00078

Zou L, Ravet F, Bao X, Chen L (2004) Highly precise distributed Brillouin scattering sensor for structural health monitoring of optical ground wire cable. Smart Structures and Materials: Sensors and Smart Structures Technologies for Civil, Mechanical, and Aerospace Systems *5391:* 293-300. https://doi.org/10.1117/12.540193

Zhang G, Xing Y, Wang L (2018) Comprehensive sandstone fracturing characterization: Integration of fiber Bragg grating, digital imaging correlation and acoustic emission measurements. Eng Geol 246: 45-56. https://doi.org/10.1016/j.enggeo.2018.09.016

Zhang L, Yang D, Chen Z, Liu A (2020) Deformation and failure characteristics of sandstone under uniaxial compression using distributed fiber optic strain sensing. J Rock Mech Geotech 12(5): 1046-1055. https://doi.org/10.1016/j.jrmge.2019.12.015

Zhou XP, Zhao Z, Liu Y (2020) Digital spatial cracking behaviors of fine-grained sandstone with precracks under uniaxial compression. Int J Numer Anal Met 44(13): 1770-1787. https://doi.org/10.1002/nag.3088

Abbreviations

UCS	Uniaxial compressive strength
ESG	Electrical resistance strain gauge
LVDT	Linear variable differential transformer
FBG	Fibre Bragg grating
DIC	Digital image correlation
SHM	Structural health monitoring
DFOS	Distributed fibre optic sensing
OFDR	Optical frequency domain reflectometry
COD	Crack opening displacement
AE	Acoustic emission

List of Symbols

$\Delta\nu$	Rayleigh spectrum shift
$\Delta\varepsilon$	Strain change in the fibre
ΔT	Temperature change for the fibre
C_ε, C_T	Constants related to strain change and temperature change in OFDR system
ε_L , ε_A , ε_v	Lateral strain, axial strain, and volumetric strain
θ , θ_1 , θ_2	Inclined angles of the optical fibres
ε_1 , ε_2	Measured strains in the fibre
υ	Poisson's ratio of the specimens' maternal
arctan	Inverse tangent function
σ_{cd}	Crack damage stress threshold
σ_{ucs}	Uniaxial compressive strength
ε_{rock}	Uniform lateral strain on the rock surface
λ	Strain lag parameter
i	Serial number of cracks
n	Total numbers of cracks
x_i	The position of a crack at a given x coordinate
G_e	Shear modulus of the epoxy adhesive

E_f	Elastic modulus of the fibre core
r_f, r_e	Radii of the fibre core and epoxy adhesive layer
R	Strain transferring rate
L	Bonding length of the measuring fibre
x	Distance from the midpoint of the measuring fibre

Figure Caption List

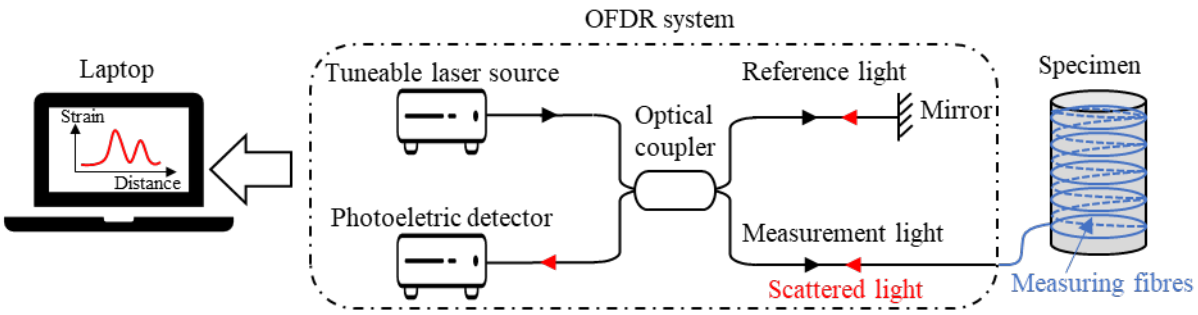

(a)

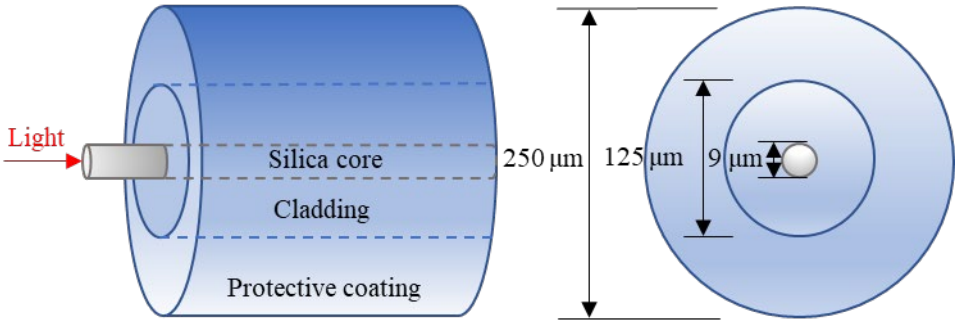

(b)

Figure 1. Composition of the measurement system: (a) OFDR system and (b) Corning SMF-28E(R) fibre

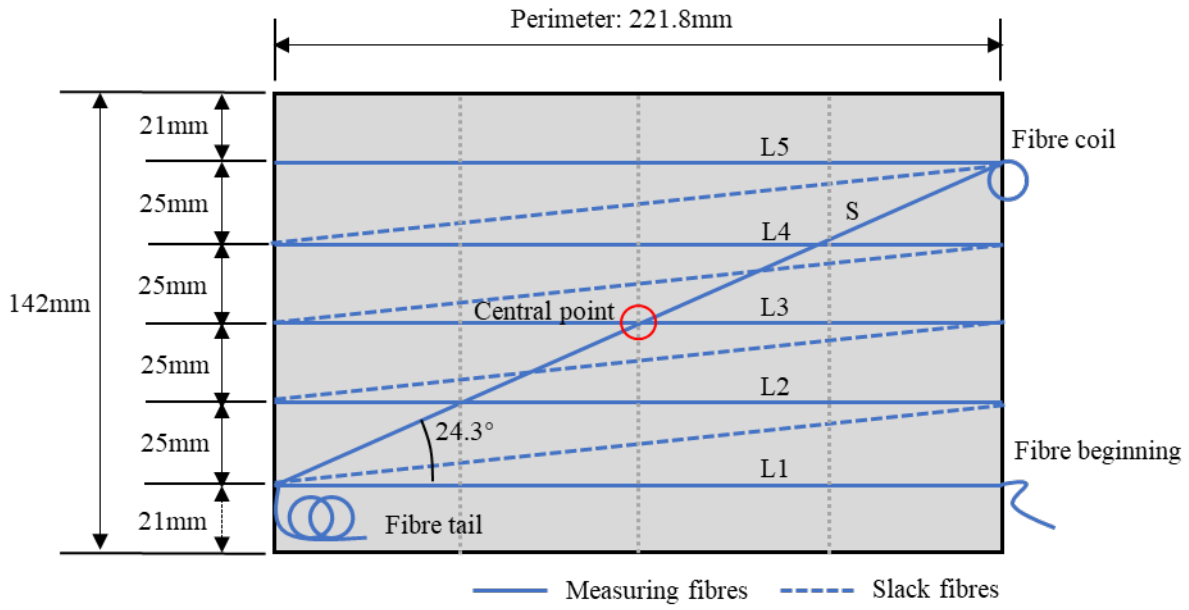

(a)

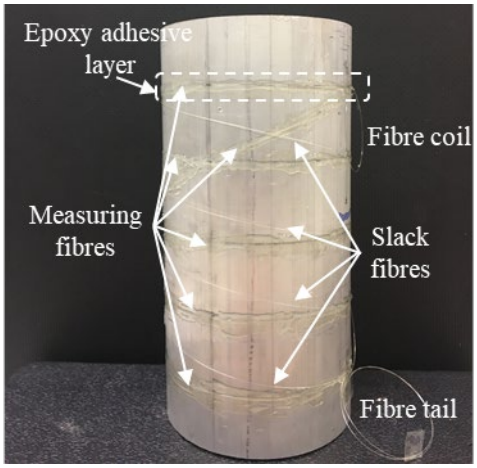

(b)

Figure 2. Details of the UCS test on the aluminium alloy specimen: (a) surface layout of measuring fibres and (b) specimen photograph

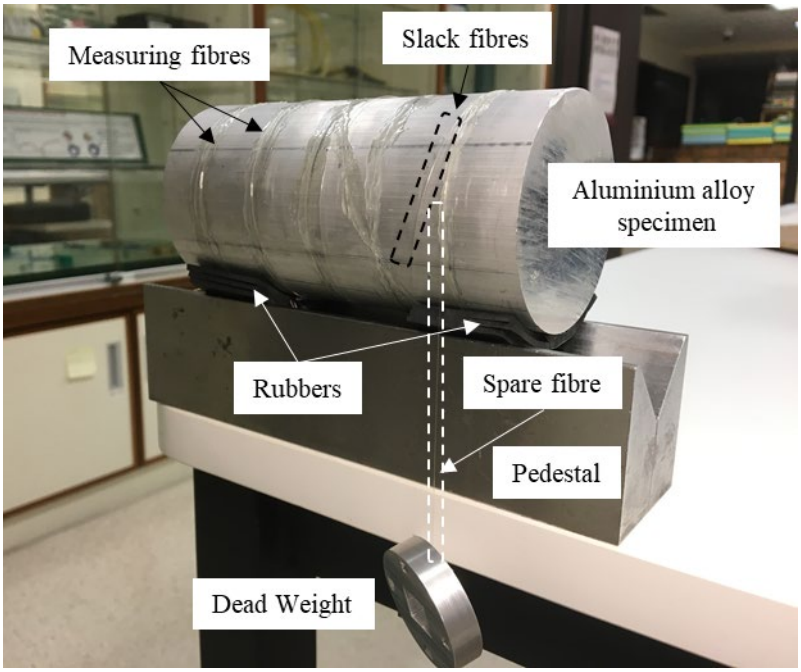

Figure 3. Photograph of the designed platform for fibre installation

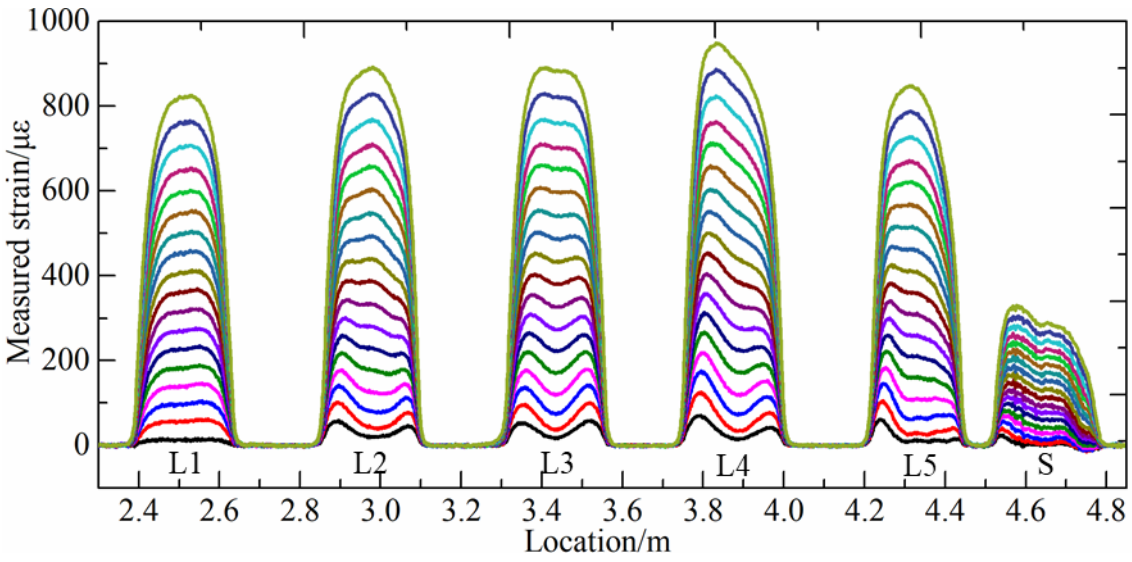

(a)

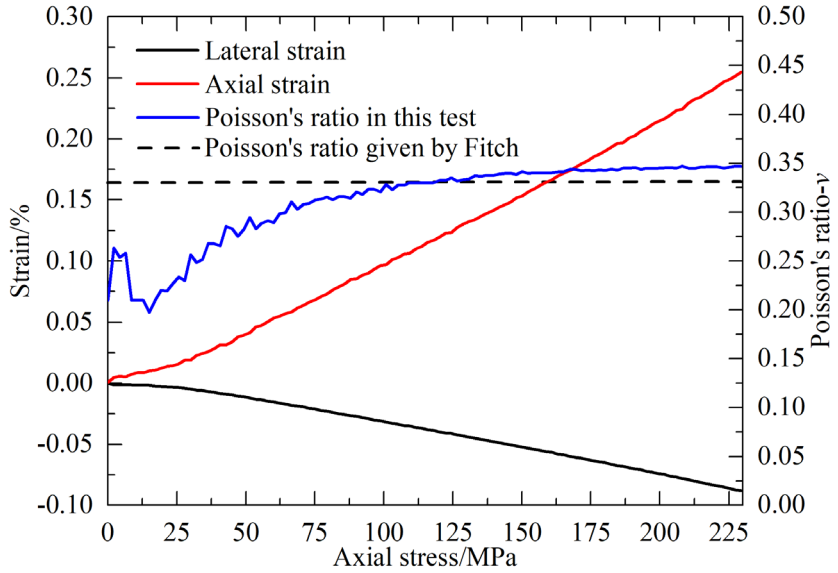

(b)

Figure 4. Test results for the aluminium alloy specimen: (a) strain profiles of fibres and (b) strain-stress and υ-stress under uniaxial compression (Fitch 1963)

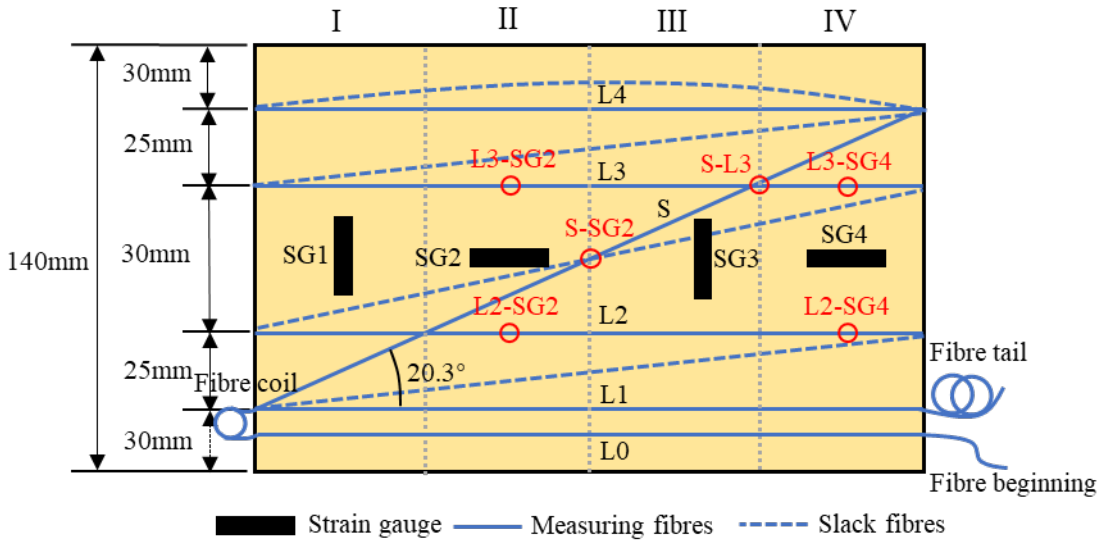

(a)

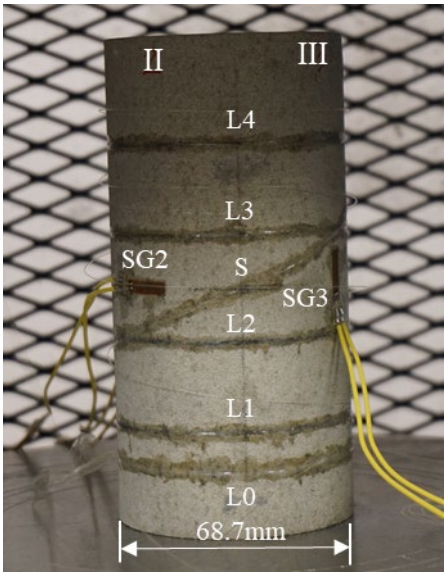

(b)

Figure 5. (a) Schematic diagram of the layout of the measuring fibres and strain gauges on the sandstone surface and (b) photograph of the sandstone specimen

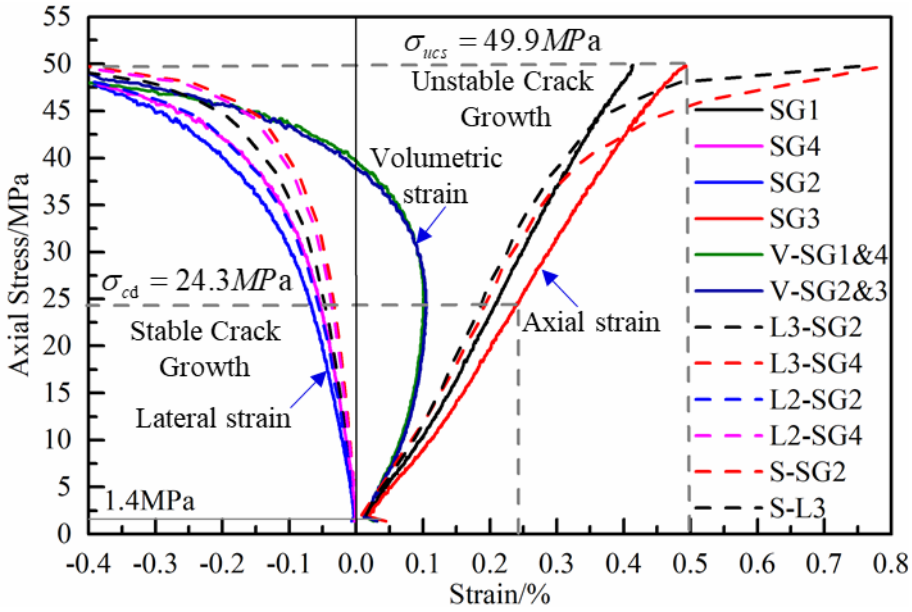

Figure 6. Stress-strain diagram measured by strain gauges and fibres during the UCS test on the sandstone specimen

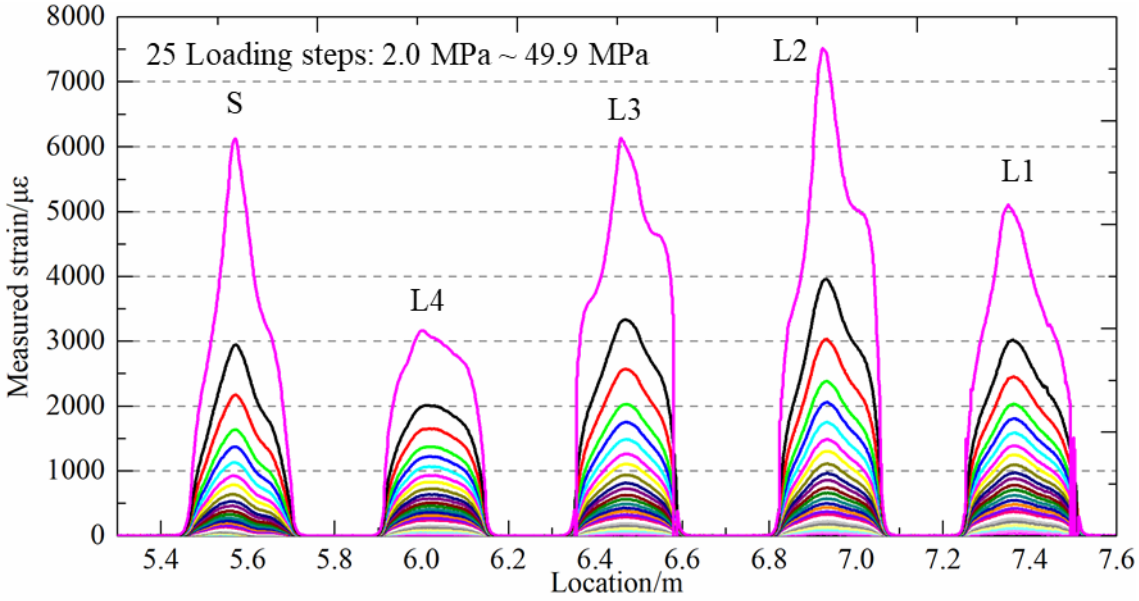

Figure 7. Measured strain profiles from five measuring fibres

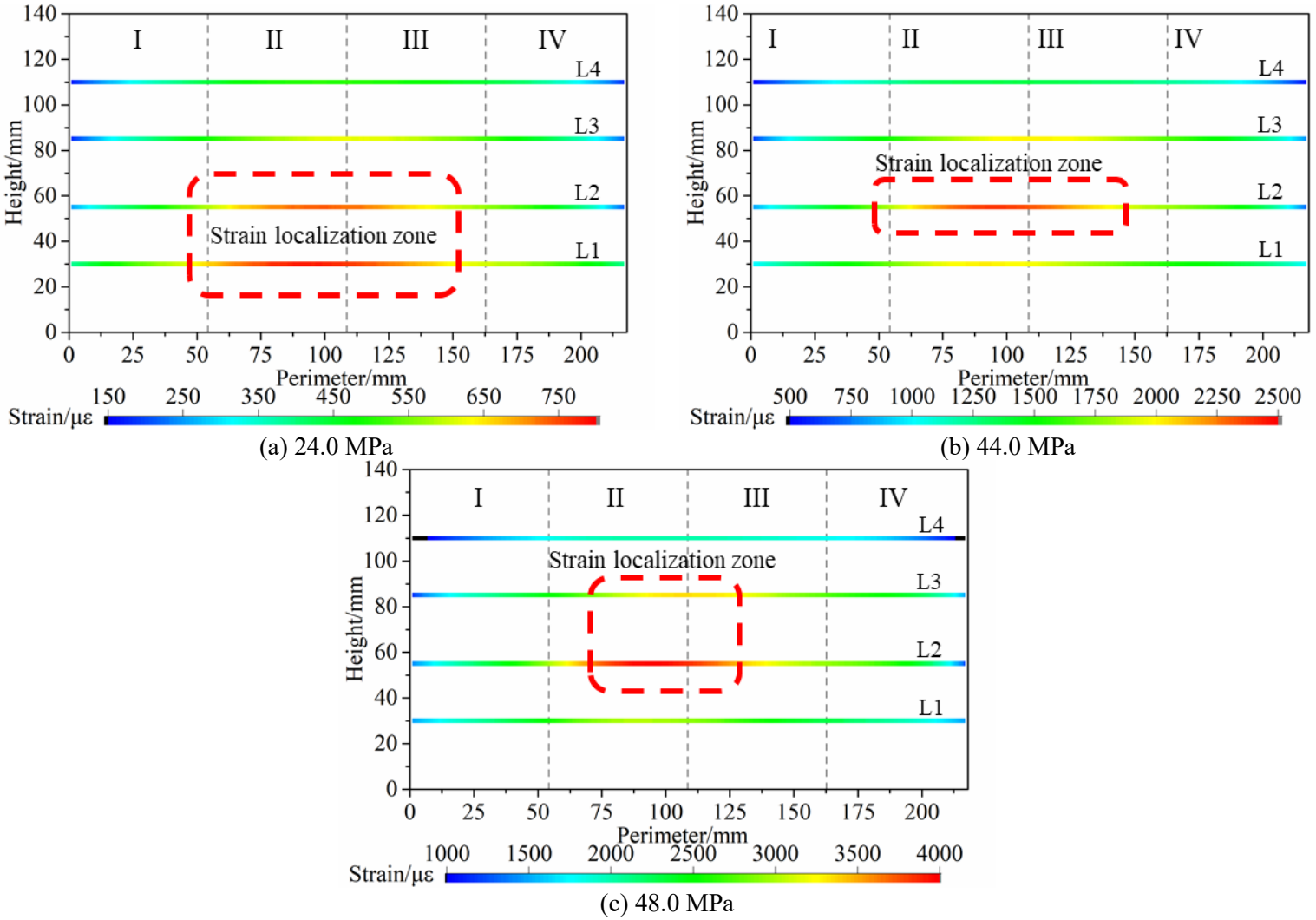

Figure 8. Three typical strain distributions for the sandstone specimen

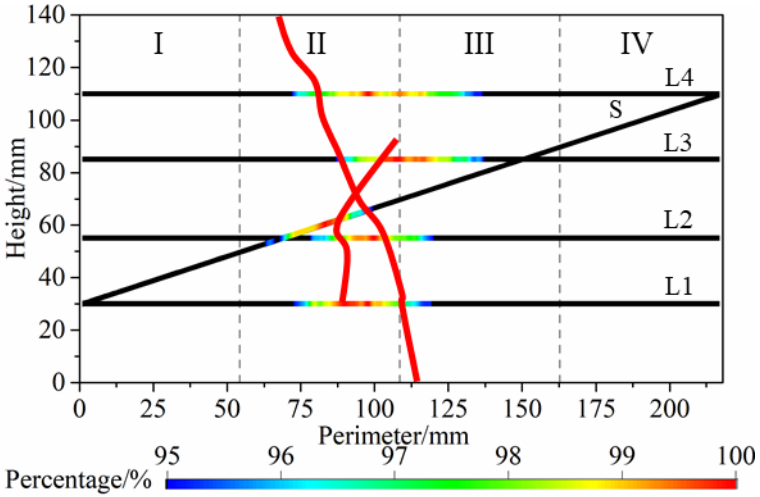

(a) 24.0 MPa

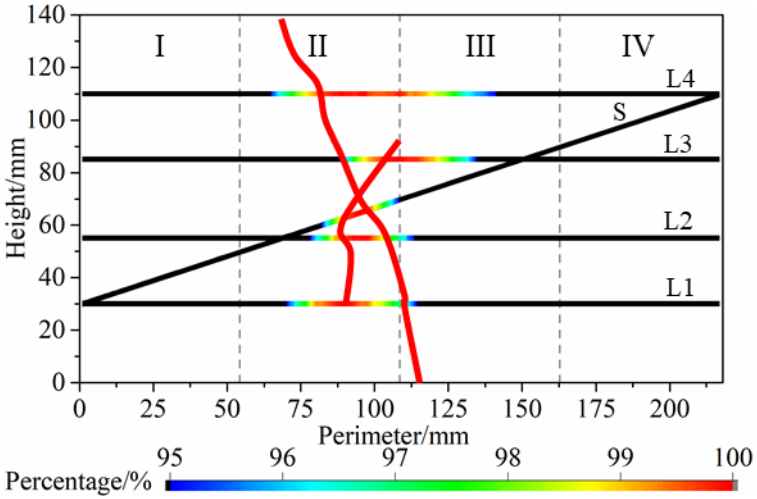

(b) 48.0 MPa

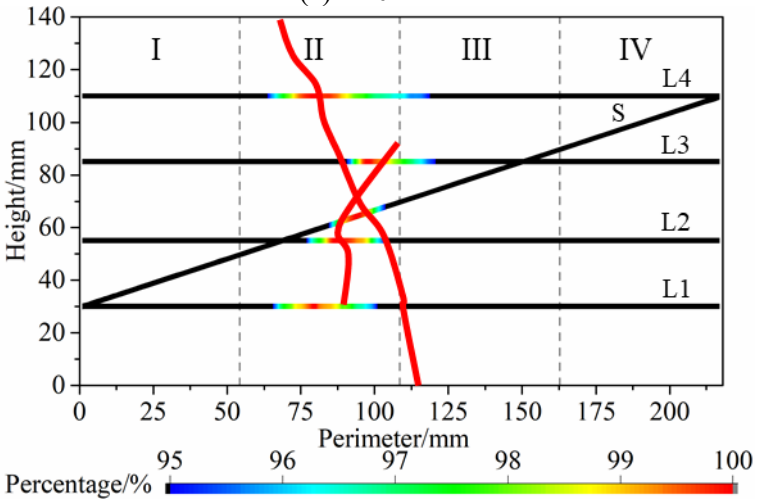

(c) 49.9 MPa

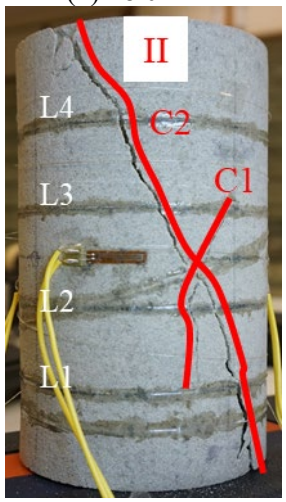

(d) failure of II region

Figure 9. Strain localization characteristics at different heights in the sandstone under different axial stresses and a photograph of the sandstone failure

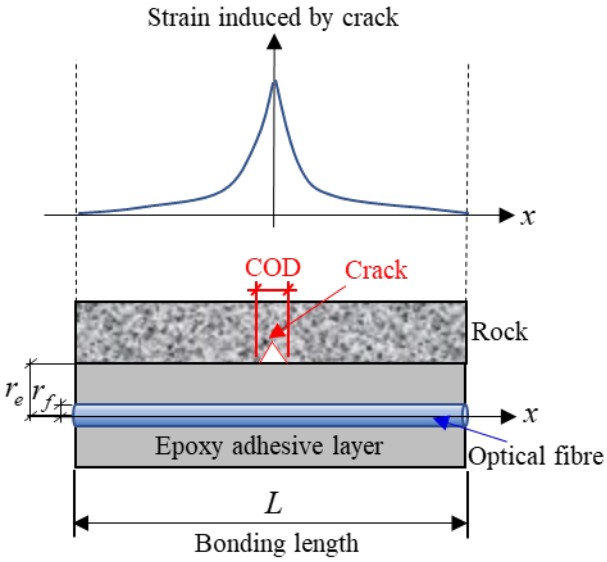
Strain induced by crack
x
COD
Crack
Rock
r_e
r_f
x
Epoxy adhesive layer
Optical fibre
L
Bonding length

(a)

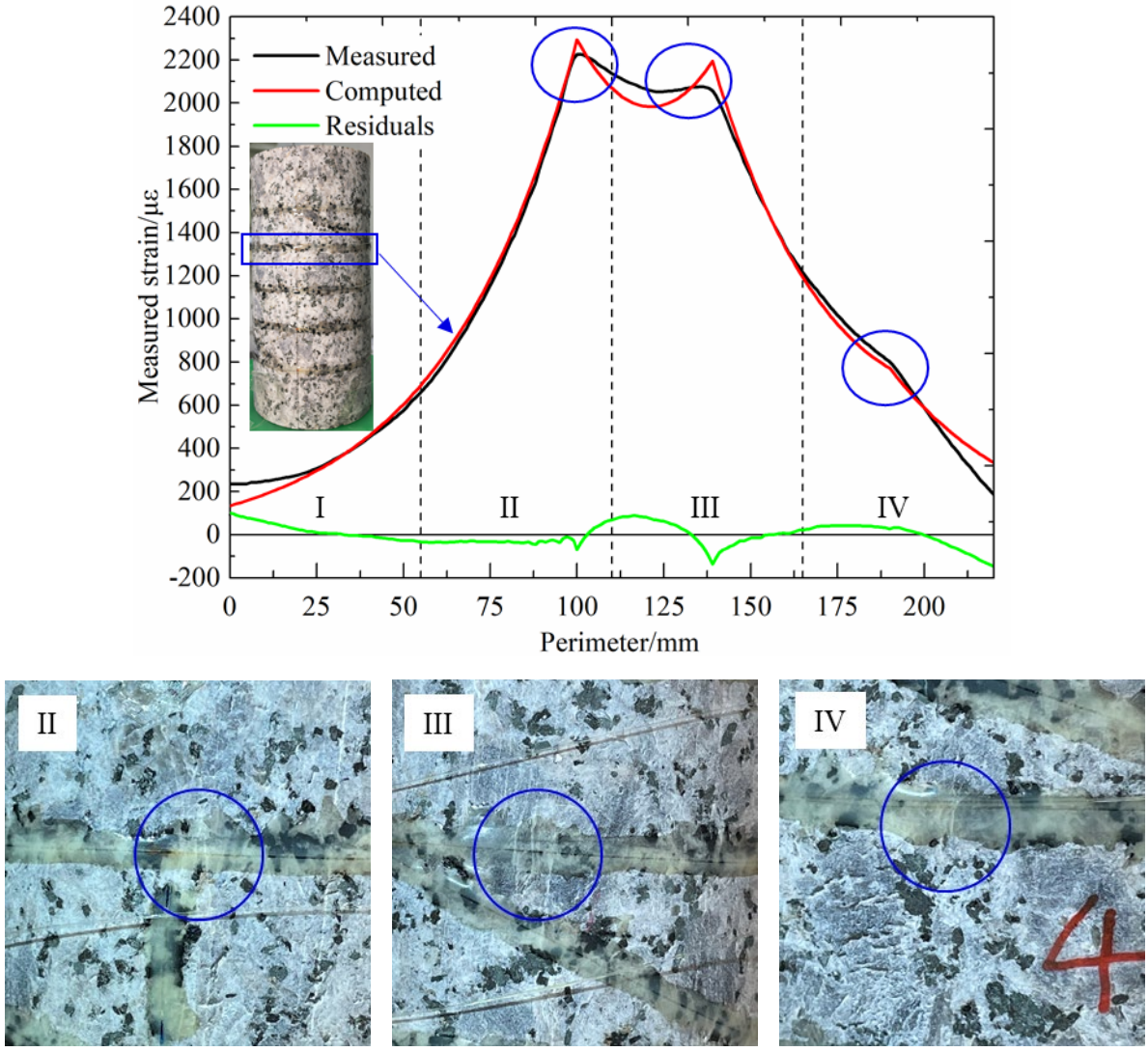
Measured
Computed
Residuals
Measured strain/με
Perimeter/mm
I
II
III
IV
II
III
IV

(b)

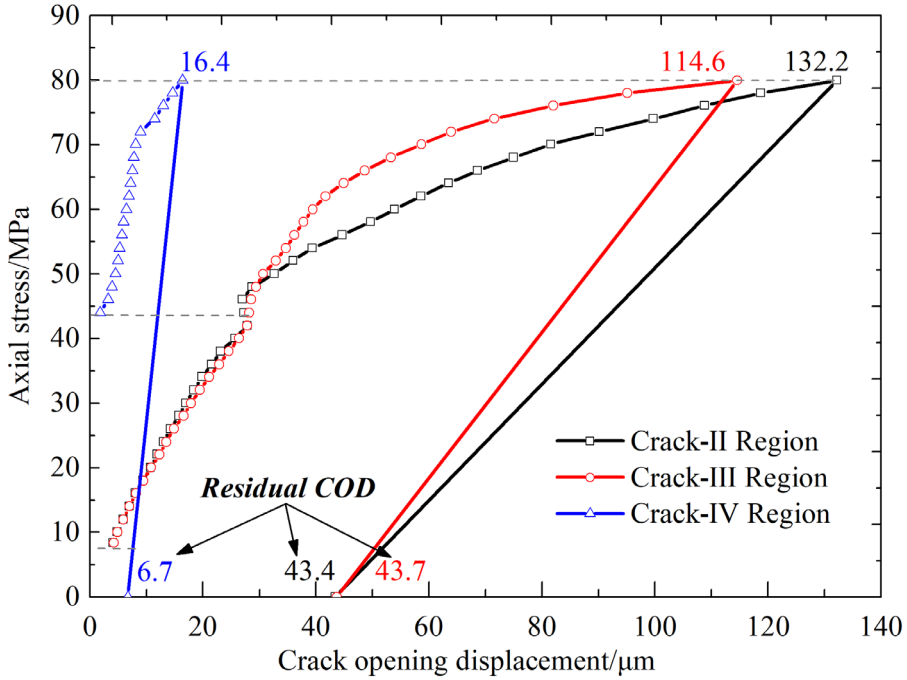

Figure 10. Quantification of crack opening displacement for the granite sample: (a) strain transfer on a fractured rock surface, (b) measured and computed strain of a surface measuring fibre and strain residuals, and (c) COD development of three cracks

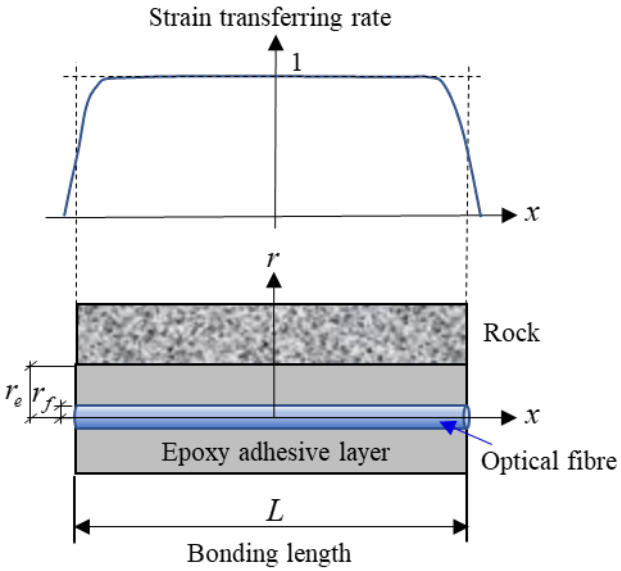

(a)

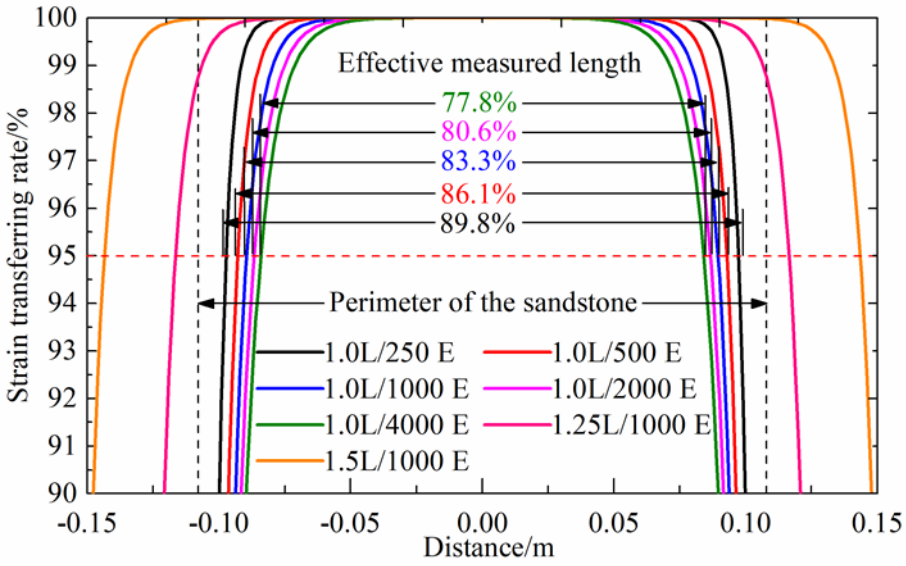

(b)

Figure 11. (a) Strain transfer rate on an intact rock surface and (b) sensitivity analysis of strain transfer rate along the measuring fibre

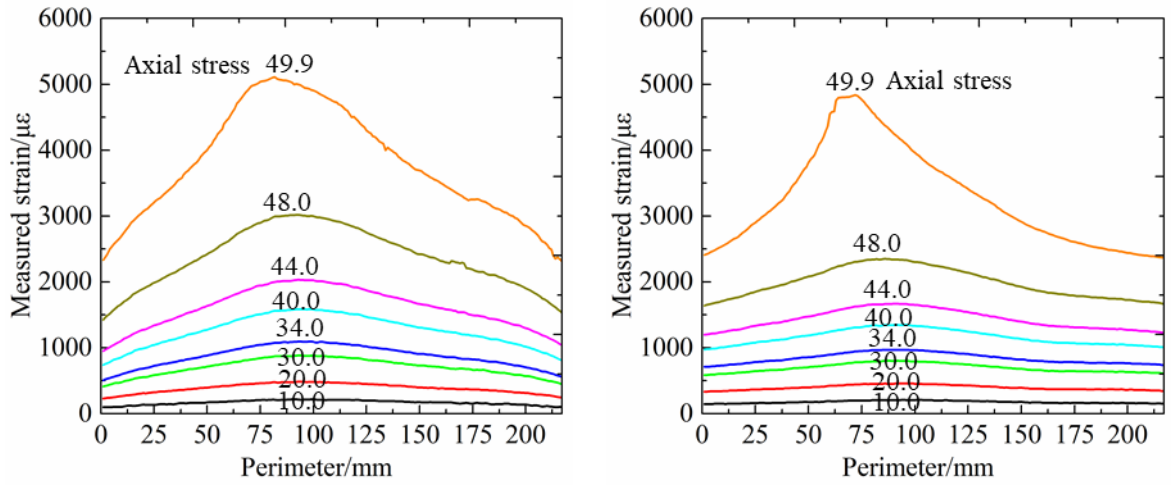

Figure 12. Distribution profiles of measurements of two fibres with different bonding lengths: (a) 'L1' fibre and (b) 'L0' fibre

1

Table 1. Values of the parameters for the measuring fibres

Materials properties	Symbols	Values	Unit
Young's modulus of fibre core	E_f	73	GPa
Radius of optical fibre (see Fig. 10a)	r_f	0.125	mm
Shear modulus of the epoxy adhesive layer	G_e	31	MPa
Radius of the epoxy adhesive layer	r_e	1.0	mm

Table 2. Combinations of values for sensitivity analysis of strain transfer rate

Name	Radius of the epoxy adhesive layer r_e / mm	Bonding length/ mm
1.0L/250 E	0.25	215.8
1.0L/500 E	0.5	215.8
1.0L/1000 E	1.0	215.8
1.0L/2000 E	2.0	215.8
1.0L/4000 E	4.0	215.8
1.25L/1000 E	1.0	269.8
1.5L/1000 E	1.0	323.7